nature materials

Supplementary information

https://doi.org/10.1038/s41563-026-02731-2

Tuning moiré twist angles enhances tensile plasticity in bulk van der Waals crystals

In the format provided by the authors and unedited

Table of Contents

Including:

Supplementary Note

Understanding on high hole mobility

Based on the deformation potential theory[1], the carrier mobility can be simply evaluated using

$$\mu = \frac{(8\pi)^{1/2} e\hbar^4 c_{ii}}{3(m^*)^{5/2}(k_B T)^{3/2}\Xi^2},$$

where e is the element charge, $\hbar$ is the reduced Planck constant, c_{ii} is the elastic constant, m^* is the effective mass, Ξ is the deformation potential, k_B is the Boltzmann constant, and T is the temperature. The deformation potential (Ξ), defined as the change in band energy position (ΔE) relative to a small change in lattice length (Δl) along a specific lattice direction (l_0), can be evaluated by $\Xi=\Delta E/(\Delta l/l_0)$. To take into account the nonparabolic and multiple band behaviors of the near-edge band structures, the effective mass was calculated from the theoretical electrical conductivity using Boltzmann transport calculations in the BoltzTraP code based on the full *ab initio* band structures[2,3]. Well-converged electronic structure of bulk GaGeTe was calculated using the TB-mBJ method[4] implemented in VASP, where a 500 eV plane wave energy cutoff, an energy convergence criterion of 10^{-6} eV, and a dense *k*-mesh of 33×33×33 were adopted for the calculation. The deformation potential was calculated by the TB-mBJ method using the change in the valence band maximum with a small in-plane lattice dilation. The elastic constant was calculated with the PBE-D3(BJ) method. Both electron and hole effective masses were calculated to be small, ~0.27m_e, suggesting the potential of achieving high carrier mobility. Considering the anisotropy, the hole effective mass within the *a*-*b* plane is about 0.76m_e, much larger than that of ~0.12m_e along the *c* axis. This can be understood by the dominant contribution of p_z orbitals of Ga, Ge, and Te atoms at the valence band maximum, which results in larger orbital overlap and lighter effective mass along the *c* axis. However, a large in-plane elastic constant of ~88.7 GPa and a small deformation potential (~2 eV) result in a high calculated in-plane hole mobility of ~2691 $cm^2 V^{-1} s^{-1}$, indicating the potential for high hole mobility.

The intrinsic carrier mobility is closely related to near-edge electronic bands. To understand the impact of moiré twisting deformation on mobility, we first calculated the in-plane band structures of moiré supercells θ-GaGeTe (θ = 0° and 21.79°) using the PBE functional, which provides sufficiently large band gaps (Supplementary Fig. 9d). The results reveal that the near-edge electronic bands, particularly the valence band maximum, exhibit minimal changes with varying twist angles. This finding aligns with the experimental observation that plastic deformation through twisting has a negligible impact on in-plane mobility. This is understandable, as the

twisting primarily involves the relative rotation of entire layers without disrupting the intralayer atomic structure. Moreover, the valence band maximum is mainly derived from the p_z orbitals of intralayer atoms (Supplementary Fig. 10), and the orbital overlap is thereby largely unaffected by the twisting between layers, resulting in minimal changes to the effective mass of the valence band maximum. These results provide further confirmation that moiré twisting does not significantly affect in-plane carrier mobility, reinforcing the stability of electronic properties during deformation.

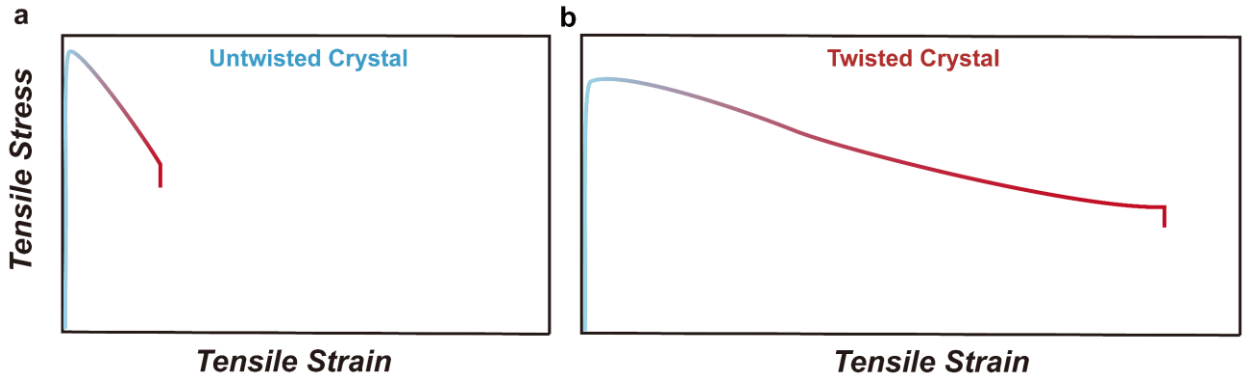

Supplementary Fig. 1 | Schematics of the tensile stress versus strain curves of untwisted and twisted crystals. Moiré twisting in twisted crystals is introduced by off-axis pre-compression (10% compressive strain with ~5° off-axis angle).

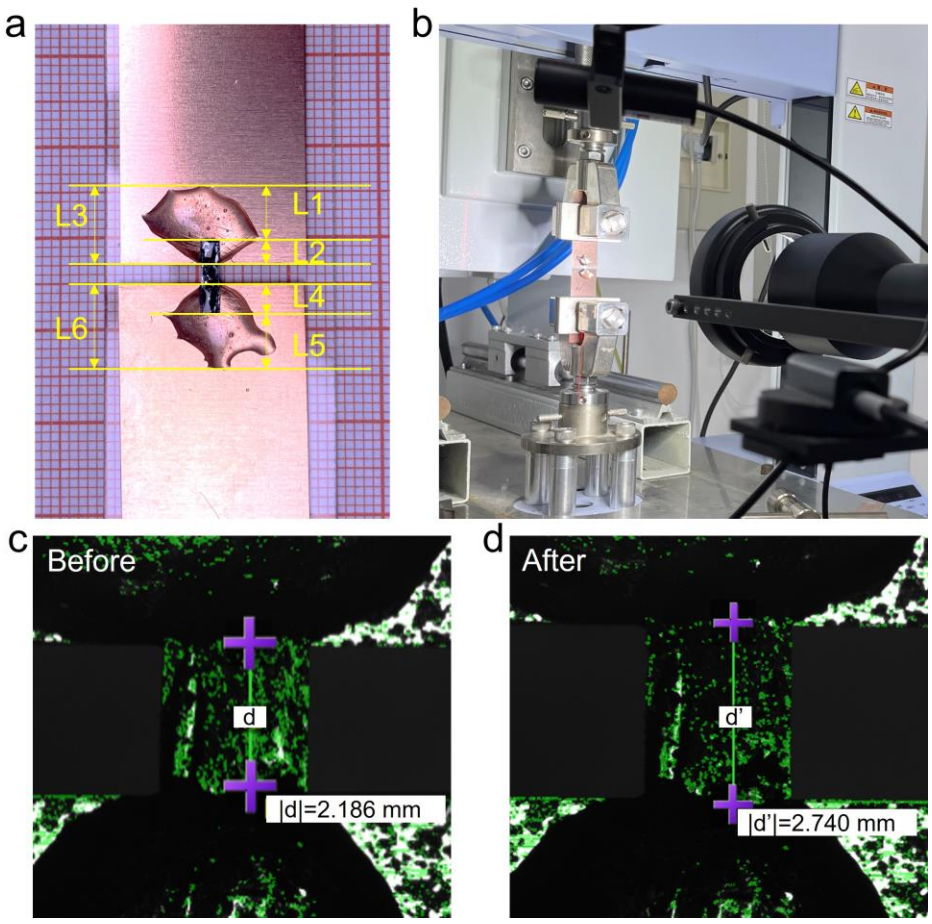

Supplementary Fig. 2 | **a,** Photograph of the GaGeTe sample mounted on a copper substrate. **b,** Photograph showing the clamping configuration of the sample-copper assembly in the universal testing machine. **c,d,** Digital images of the GaGeTe sample with tracking markers before (**c**) and after (**d**) tensile tests.

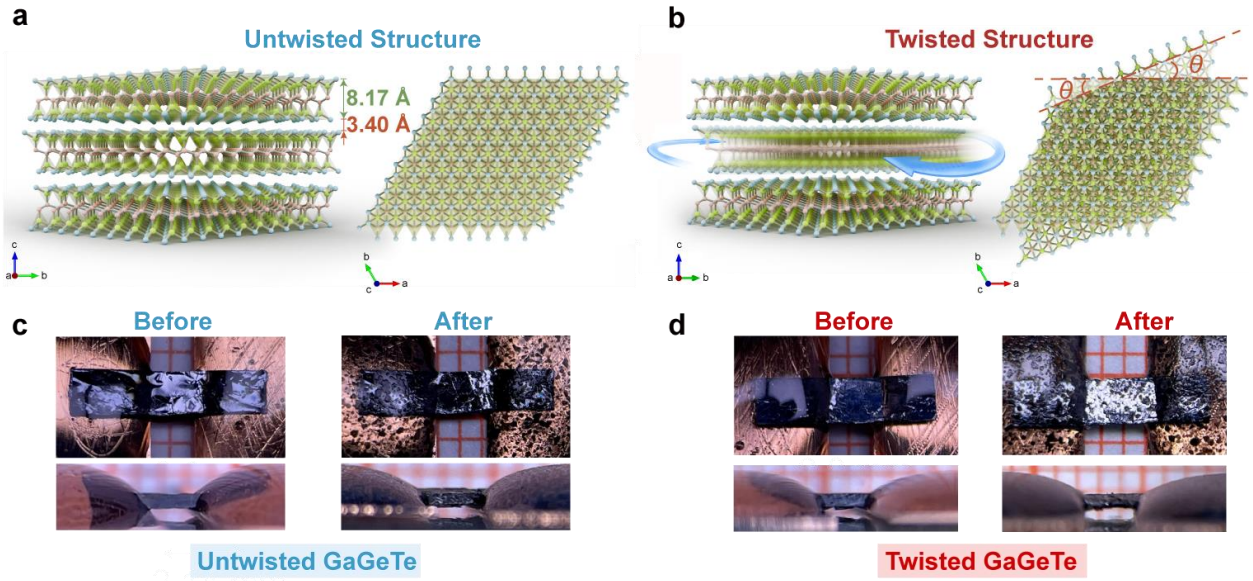

Supplementary Fig. 3 | a,b, Illustration of untwisted (**a**) and twisted-layer (**b**) crystal structures of GaGeTe. **c,d,** Optical images of the untwisted (**c**) and twisted (**d**) GaGeTe crystals before and after tensile testing.

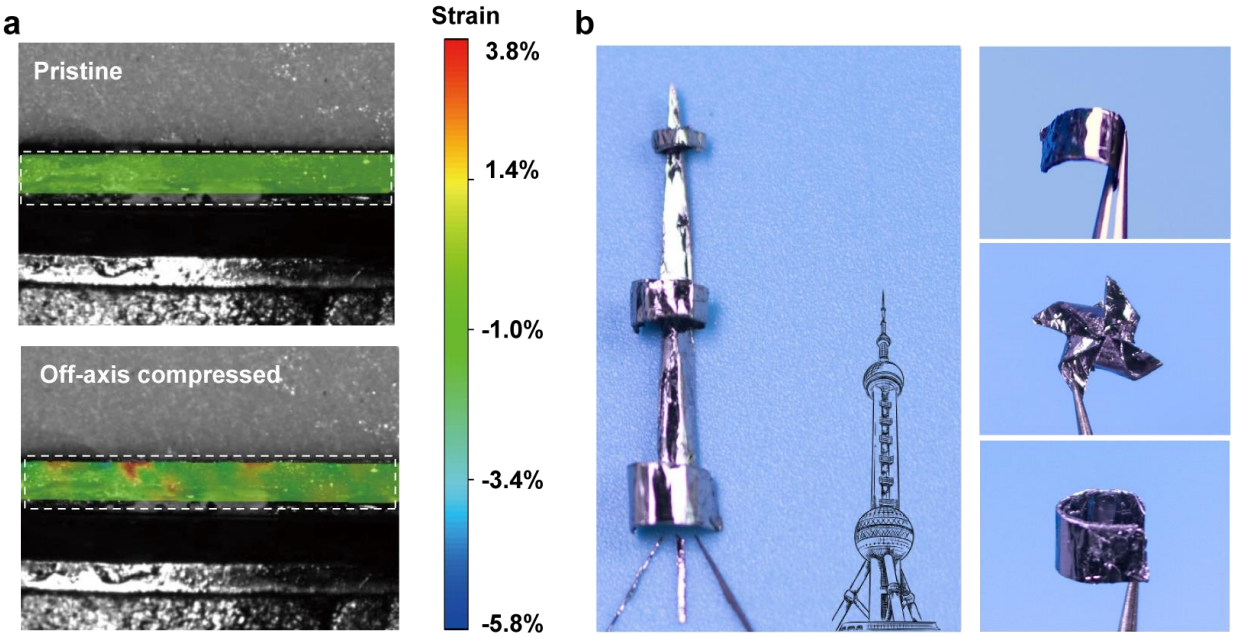

Supplementary Fig. 4 | a,b, Strain distribution during the off-axis compressive tests of GaGeTe bulk crystal (**a**) and optical images of the twisted GaGeTe crystals morphed into various shapes (**b**).

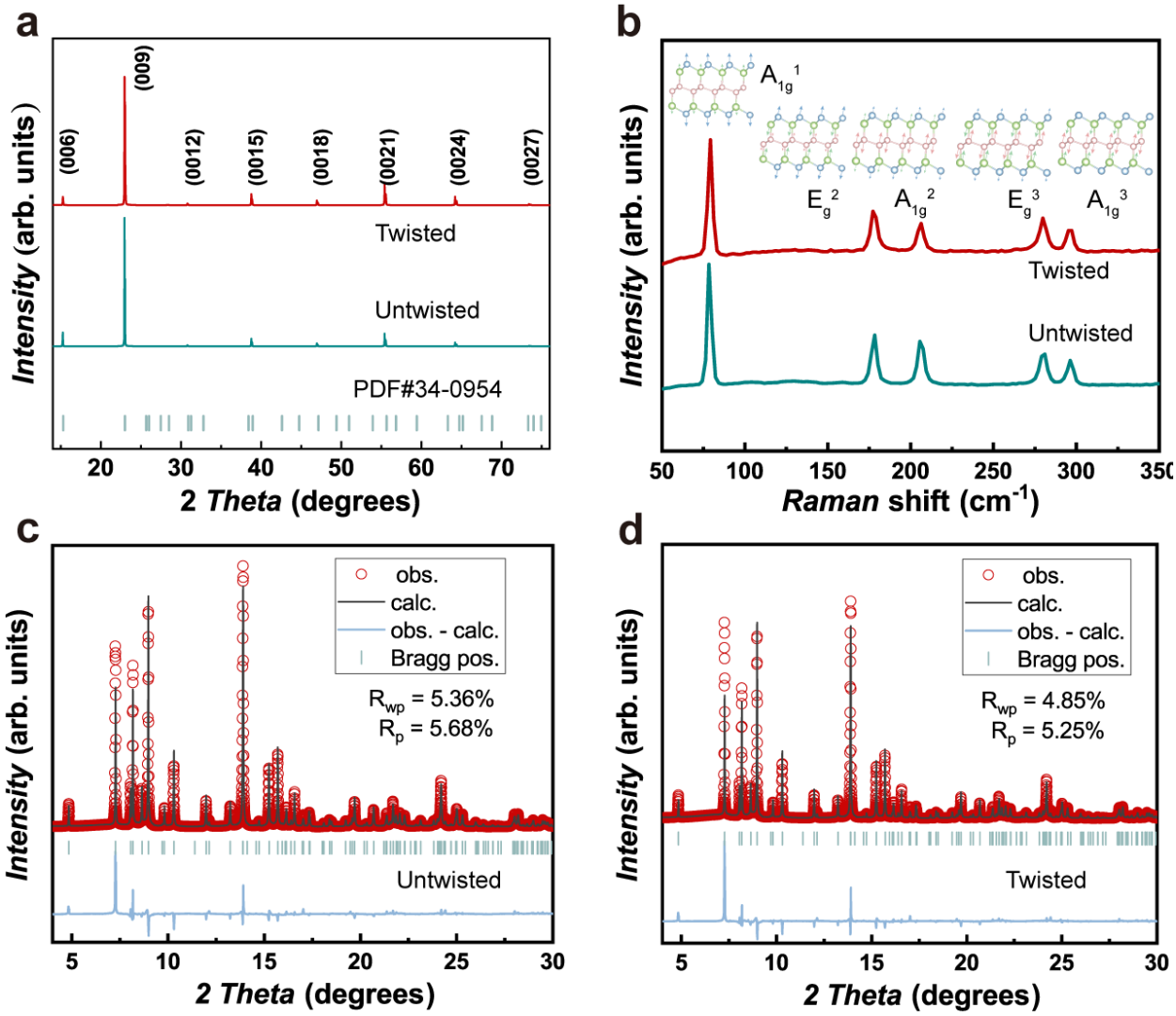

Supplementary Fig. 5 | The structural evolution of GaGeTe after mechanical deformation. **a,b,** XRD and Raman spectra results of untwisted (green) and twisted (red) bulk samples. **c,d,** Synchrotron PXRD data at 300 K of untwisted (**c**) and twisted (**d**) samples, along with Rietveld refinements.

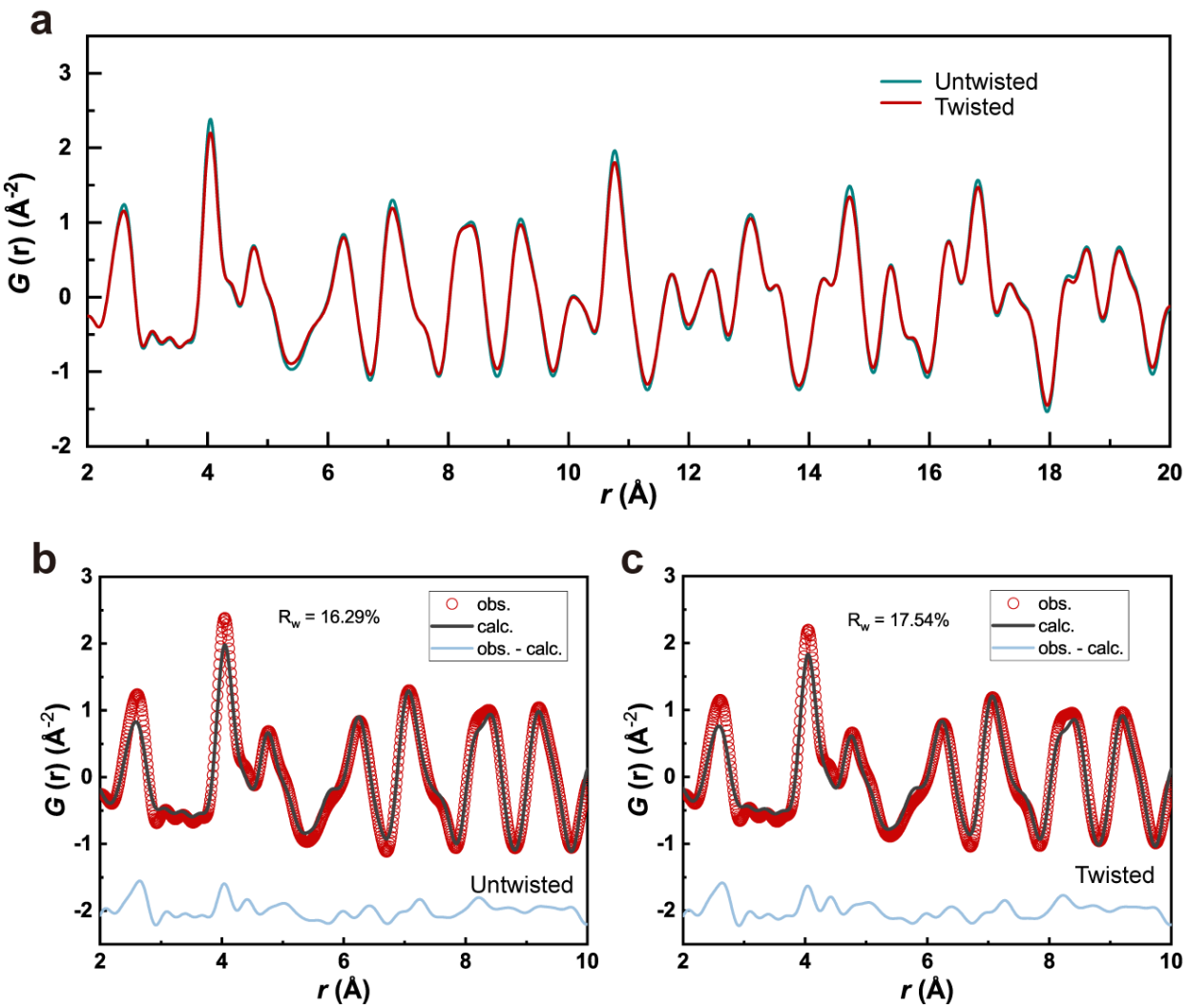

Supplementary Fig. 6 | The local structural evolution of GaGeTe after mechanical deformation. **a,** The comparison of the experimental X-ray PDF data at 300 K of untwisted and twisted samples. **b,c,** The refinements of synchrotron PDF data at 300 K of the untwisted (**b**) and twisted (**c**) samples with R$\bar{3}$m model.

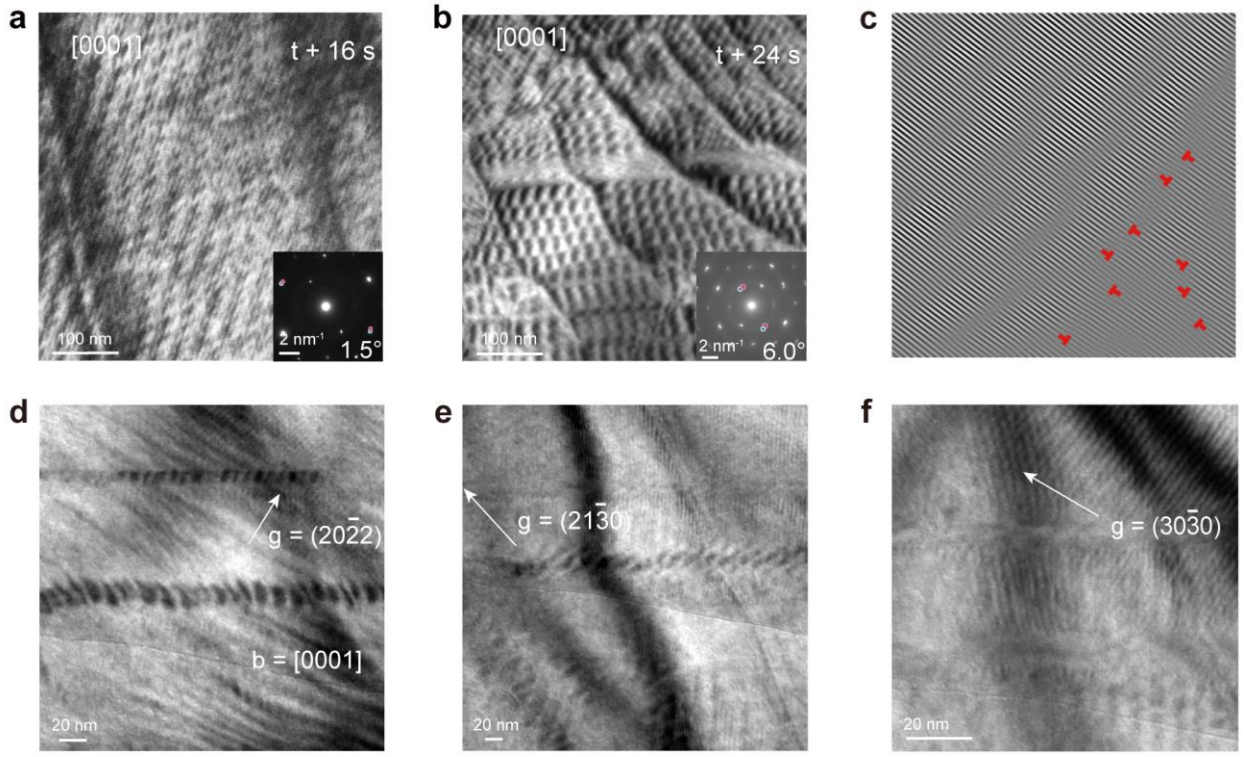

Supplementary Fig. 7 | Moiré superlattice with the angles at about 1.5° and 6.0°, and bright-field TEM images captured from Supplementary videos 1, 2, and 3 during in-situ TEM tensile tests of GaGeTe. a,b, TEM images taken during in-situ TEM tensile tests, capturing clear moiré patterns and periodic lengths with the insets (SAED) indicating the moiré twisting angles between two sets of diffraction spots are 1.5° (**a**) and 6.0° (**b**), respectively. Times listed are relative to the beginning of the Supplementary videos 1 and 2, respectively. **c-f,** The dislocation (**c**) and g·b analysis were taken at different g vectors: (**d**) g = (20$\bar{2}$2), (**e**) g = (21$\bar{3}$0), (**f**) g = (30$\bar{3}$0).

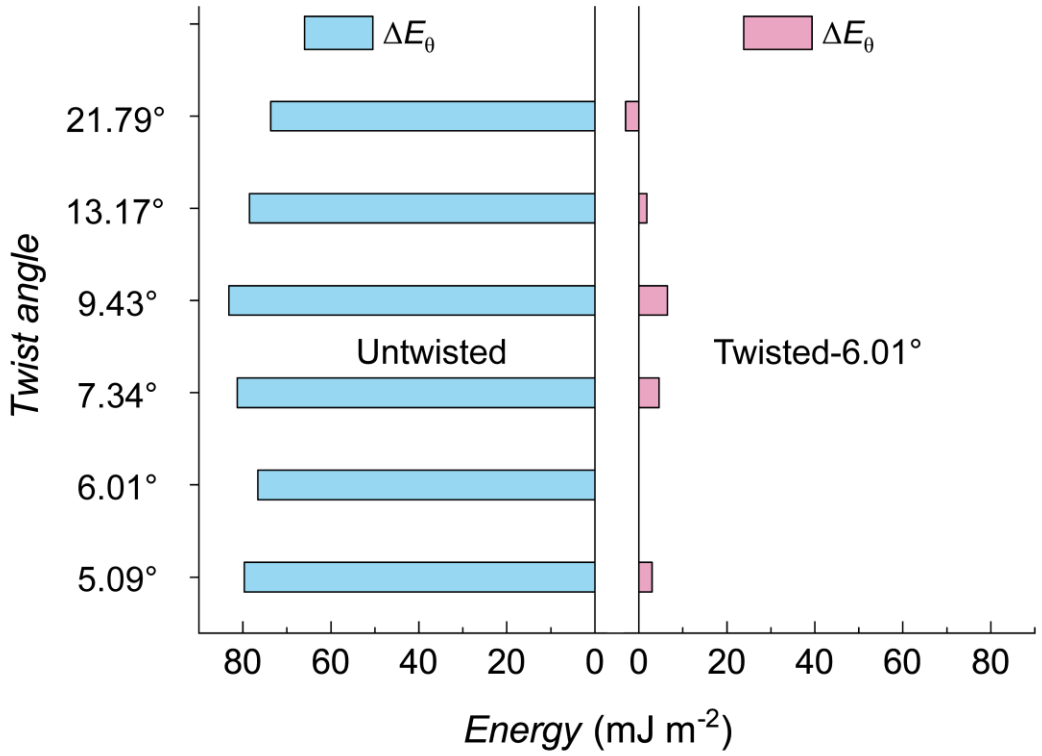

Supplementary Fig. 8 | The calculated formation energy ΔE_θ for the twisted GaGeTe (θ-GaGeTe) with untwisted (θ = 0°) and θ = 6.01° as the original states, respectively.

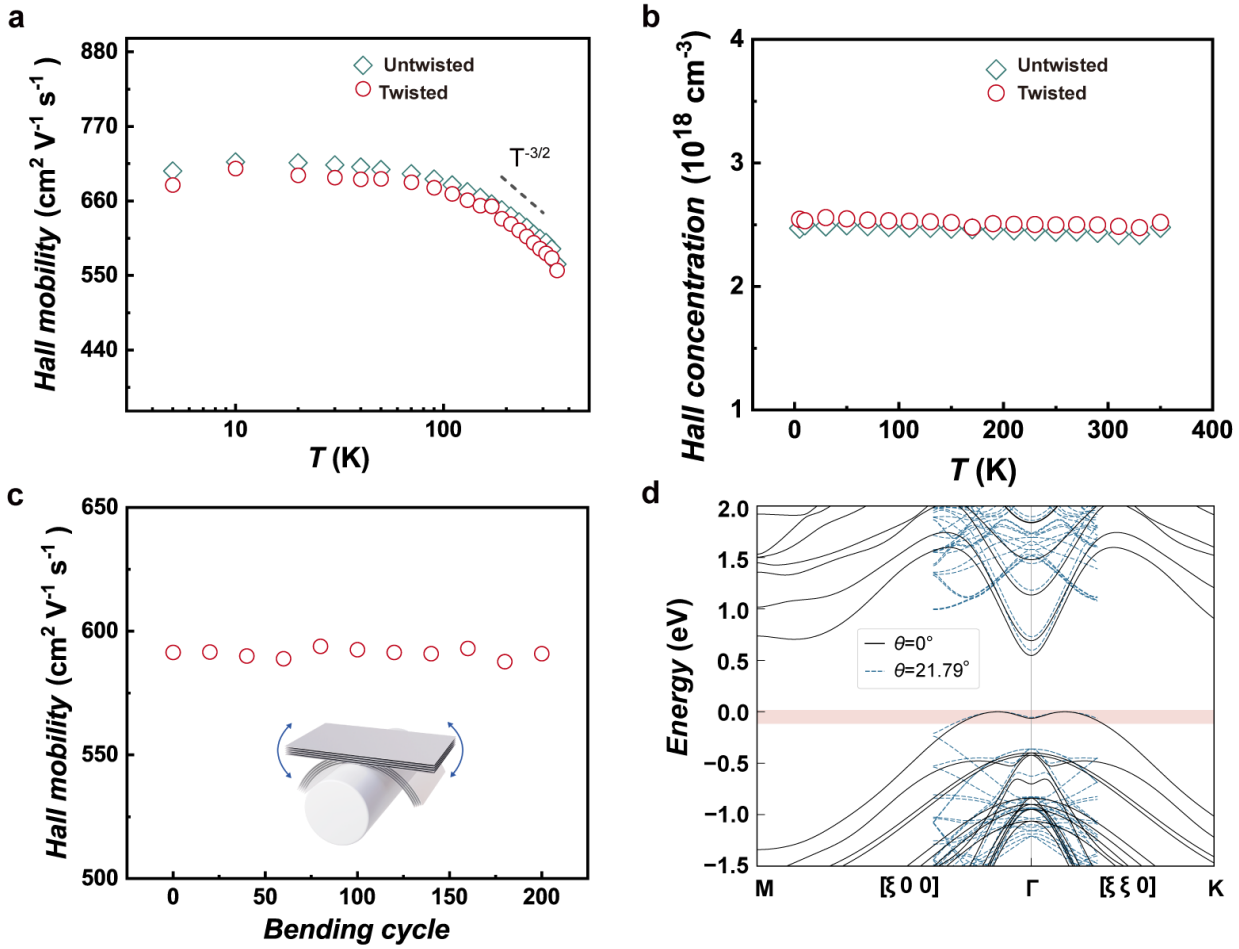

Supplementary Fig. 9 | The influence of plastic deformation on Hall mobility. a,b, Temperature-dependent μ_H (**a**) and p_H (**b**) of untwisted and twisted (off-axis compressed) bulk single-crystalline GaGeTe along the in-plane direction. **c,** μ_H variation of the bulk single crystal GaGeTe during a few hundred bending cycles. The bending radius is 10 mm. After each bending, the single crystal is restored to its initial shape for the next bending cycle. **d,** In-plane band structures of moiré supercells of GaGeTe with twist angles of θ = 0° and 21.79°. The valence band maximum is set to 0 eV. The pink region highlights the near-edge valence bands.

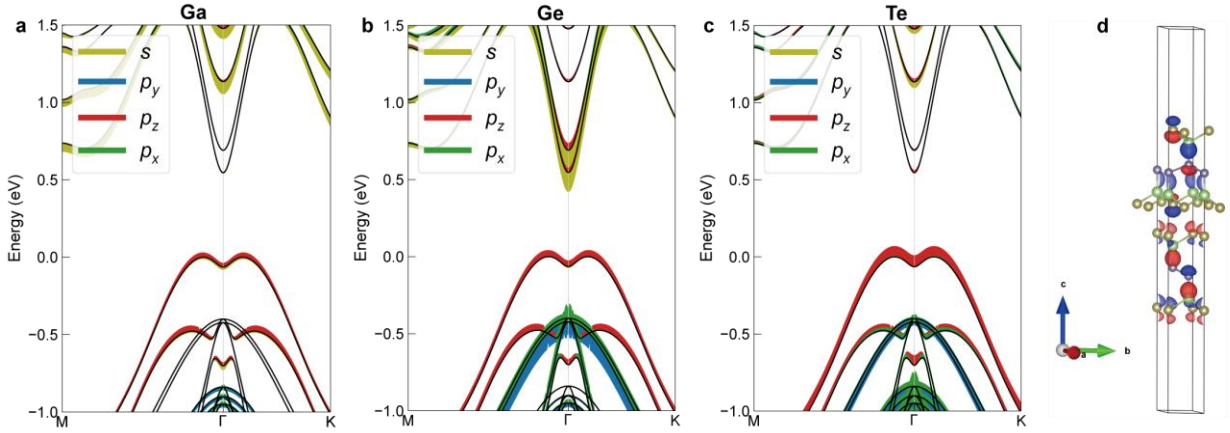

Supplementary Fig. 10 | Orbital-resolved in-plane band structures of (a) Ga, (b) Ge, and (c) Te atoms in the untwisted moiré supercell of GaGeTe. The valence band maximum is set to 0 eV. **d,** Real-space wave function plot at the valence band maximum.

Supplementary Table 1. The actual dimensions of each individual sample in Fig. 1a,b and Extended Data Fig. 10.

Compositions			Actual Sizes (mm)		
			Width	Height	Length
GaGeTe	Pristine	Sample1	1.899	0.462	8.000
		Sample2	1.971	0.542	8.001
		Sample3	2.098	0.517	8.001
		Sample4	2.095	0.503	8.006
		Sample5	2.088	0.520	8.010
	Off-axis compressed	Sample1	2.022	0.512	8.001
		Sample2	1.880	0.615	8.000
		Sample3	1.976	0.610	8.004
		Sample4	1.967	0.468	7.988
		Sample5	2.185	0.533	8.005
$CrSiTe_3$	Pristine		1.950	0.437	7.865
	Off-axis compressed		1.970	0.466	7.870
$InSiTe_3$	Pristine		1.883	0.428	7.954
	Off-axis compressed		1.985	0.528	8.000
$SnBi_2Te_4$	Pristine		2.175	0.492	8.208
	Off-axis compressed		1.851	0.578	8.220
InSe	Pristine		2.343	0.452	7.886
	Off-axis compressed		2.449	0.501	7.885
GaS	Pristine		1.905	0.438	7.940
	Off-axis compressed		1.887	0.625	7.929
GaSe	Pristine		1.952	0.402	7.900
	Off-axis compressed		1.910	0.467	7.898

Supplementary Table 2. Room-temperature elongation and bandgap of typical layered materials and other materials shown in Fig. 1c. The elongation data of pristine and off-axis compressed GaGeTe, $CrSiTe_3$, $InSiTe_3$, $SnBi_2Te_4$, InSe, GaS, and GaSe are from this work. Other data are taken from refs. 5-23.

Compositions	Elongation (%)		Bandgap (eV)	References
	Pristine	Off-axis compressed		
GaGeTe	8.3 ± 2.7	30.0 ± 3.3	1.12	5
$CrSiTe_3$	7.2	19.0	1.20	6
$InSiTe_3$	5.0	15.9	0.78	7
$SnBi_2Te_4$	7.1	15.0	0.49	8
InSe	7.8	15.0	1.20	9
GaS	18.2	23.8	3.00	10
GaSe	19.2	28.0	2.10	
Bi_2Te_3	8.90		0.14	11,12
MoS_2	8.84		1.30	13,14
$SnSe_2$	5.96		1.08	13,15
Ge	0.13		0.66	16,17
Si	0.09		1.12	
GaAs	0.34		1.42	
PEDOT:PSS	6.00		1.77	18,19
P3HT	10.60		2.00	20,21
HCL/PANI	11.10		2.79	22,23

Supplementary Table 3. Crystallographic data and details of the experiment and dynamical refinement of PEDT for GaGeTe at 293 K.

Composition	GaGeTe
3D ED method	PEDT
Stoichiometric formula	GaGeTe
Crystal system	Trigonal
Space group	R $\bar{3}$ m (no.166)
Lattice parameters	$a = b = 4.047(2)$ Å, $c = 35.166(9)$ Å $\alpha = \beta = 90°$ and $\gamma = 120°$ $V = 498.9(4)$ Å^3
Z	6
Thickness refined, Å	372(5)
Temperature	293 K
Radiation	0.0251 Å
Number of frames	111
Range of data collection	-59.91° to 50.09°
Tilt step	1°
Precession angle	1°
All Reflection No.	1136
Obs. Reflection No. (I > 3σ)	1101
Parameters No.	118
R_{obs}, wR_{obs}	0.0731, 0.0940
R_{all}, wR_{all}	0.0752, 0.0941

Supplementary Table 4. Refinement details of the synchrotron powder X-ray diffraction data of GaGeTe at 300 K.

Sample			Untwisted sample	Twisted sample
R_F (%)			7.76	7.10
R_{Bragg} (%)			10.49	10.74
R_p (%)			5.68	5.25
R_{wp} (%)			5.36	4.85
GaGeTe	$a = b$ (Å)		4.04722(3)	4.04719(2)
	c (Å)		34.75810(4)	34.75940(3)
	Volume (Å^3)		493.062(6)	493.072(5)
	Ga	x	0	0
		y	0	0
		z	0.25173(3)	0.25156(2)
	Ge	x	0	0
		y	0	0
		z	0.32208(3)	0.32210(1)
	Te	x	0	0
		y	0	0
		z	0.11376(2)	0.11747(1)
U_{iso} (Å^2)	Ga		0.0088(3)	0.0089(2)
	Ge		0.0073(3)	0.0076(2)
	Te		0.0080(2)	0.0088(1)
Occupancy number	Ga		0.16667	0.16667
	Ge		0.16667	0.16667
	Te		0.16667	0.16667

Supplementary Table 5. Refinement details of the synchrotron X-ray pair distribution function data of pristine and twisted GaGeTe collected at 300 K.

Sample			Untwisted sample	Twisted sample
Fit range (Å)			2-10	
R_w (%)			16.29	17.54
a=b (Å)			4.0472	4.0481
c (Å)			34.7677	34.7436
Phase scale factor			0.3503	0.3266
Quadratic atomic correlation factor			2.7281	2.5060
Crystallographic sites	Ga1		x = 0 y = 0 z = 0.25173	x = 0 y = 0 z = 0.25173
	Ge1		x = 0 y = 0 z = 0.32208	x = 0 y = 0 z = 0.32208
	Te1		x = 0 y = 0 z = 0.11738	x = 0 y = 0 z = 0.11738
ADPs (Å^2)	Ga	U_{11}	0.0099	0.0099
		U_{33}	0.0067	0.0067
	Ge	U_{11}	0.0068	0.0068
		U_{33}	0.0082	0.0082
	Te	U_{11}	0.0078	0.0078
		U_{33}	0.0084	0.0084

Supplementary Table 6. Room-temperature E_c, E_s, and E_c/E_s of typical bulk layered materials shown in Fig. 3.

Composition	E_c (mJ m^{-2})	E_s (mJ m^{-2})	E_c/E_s	References
0°-GaGeTe	331.2	34.1	9.7	This work
5.09°-GaGeTe	251.4	0.13	1933.8	
6.01°-GaGeTe	254.5	0.32	795.3	
7.34°-GaGeTe	249.9	0.17	1470.0	
9.43°-GaGeTe	248.0	0.38	652.6	
13.17°-GaGeTe	252.7	0.15	1684.7	
21.79°-GaGeTe	257.5	0.26	990.4	
$SnSe_2$	360	31.5	11.4	13
MoS_2	550	52.2	9.6	
GaSe	300	18.3	16.4	
InSe	300	19.9	15.1	

References

1 Bardeen, J. & Shockley, W. Deformation potentials and mobilities in non-polar crystals. *Phys. Rev.* **80**, 72-80 (1950).

2 Madsen, G. K. H. & Singh, D. J. BoltzTraP. A code for calculating band-structure dependent quantities. *Comput. Phys. Commun.* **175**, 67-71 (2006).

3 Lykke, L., Iversen, B. B. & Madsen, G. K. H. Electronic structure and transport in the low-temperature thermoelectric $CsBi_4Te_6$: Semiclassical transport equations. *Phys. Rev. B* **73**, 195121 (2006).

4 Tran, F. & Blaha, P. Accurate band gaps of semiconductors and insulators with a semilocal exchange-correlation potential. *Phys. Rev. Lett.* **102**, 226401 (2009).

5 Kucek, V., Drasar, C., Navratil, J., Benes, L. & Lostak, P. Optical and transport properties of GaGeTe single crystals. *J. Cryst. Growth* **380**, 72-77 (2013).

6 Casto, L. D. *et al.* Strong spin-lattice coupling in $CrSiTe_3$. *APL Mater.* **3**, 041515 (2015).

7 Chen, J. *et al.* A Submicrosecond-Response Ultraviolet–Visible–Near-Infrared Broadband Photodetector Based on 2D Tellurosilicate $InSiTe_3$. *ACS Nano* **16**, 7745-7754 (2022).

8 Zou, Y.-C. *et al.* Atomic disorders in layer structured topological insulator $SnBi_2Te_4$ nanoplates. *Nano Res.* **11**, 696-706 (2018).

9 Wei, T.-R. *et al.* Exceptional plasticity in the bulk single-crystalline van der Waals semiconductor InSe. *Science* **369**, 542-545 (2020).

10 Jung, C. S. *et al.* Red-to-Ultraviolet Emission Tuning of Two-Dimensional Gallium Sulfide/Selenide. *ACS Nano* **9**, 9585-9593 (2015).

11 Deng, T. *et al.* Room-temperature exceptional plasticity in defective Bi_2Te_3-based bulk thermoelectric crystals. *Science* **386**, 1112-1117 (2024).

12 Witting, I. T. *et al.* The Thermoelectric Properties of Bismuth Telluride. *Adv. Electron. Mater.* **5**, 1800904 (2019).

13 Gao, Z. *et al.* High-throughput screening of 2D van der Waals crystals with plastic deformability. *Nat. Commun.* **13**, 7491 (2022).

14 Lu, C.-P., Li, G., Mao, J., Wang, L.-M. & Andrei, E. Y. Bandgap, Mid-Gap States, and Gating Effects in MoS_2. *Nano Lett.* **14**, 4628-4633 (2014).

15 Deng, T. *et al.* High Thermoelectric Power Factors in Plastic/Ductile Bulk $SnSe_2$-Based Crystals. *Adv. Mater.* **36**, 2304219 (2024).

16 Faber, K. T. & Malloy, K. J. The mechanical properties of semiconductors. in *Semiconductors and Semimetals*. vol. 37 (Academic Press, 1992).

17 Springer materials. https://materials.springer.com/periodictable# (2026).

18 Liu, C. *et al.* Highly conducting free-standing poly(3,4-ethylenedioxythiophene)/poly(styrenesulfonate) films with improved thermoelectric performances. *Synth. Met.* **160**, 2481-2485 (2010).

19 Bhujel, R. *et al.* Bandgap engineering of PEDOT:PSS/rGO a hole transport layer for SiNWs hybrid solar cells. *Bull. Mater. Sci.* **44**, 72 (2021).

20 Kim, H. J. *et al.* Solution-assembled blends of regioregularity-controlled polythiophenes for coexistence of mechanical resilience and electronic performance. *ACS Appl. Mater. Interfaces* **9**, 14120-14128 (2017).

21 Ansari, M. A., Mohiuddin, S., Kandemirli, F. & Malik, M. I. Synthesis and characterization of poly(3-hexylthiophene): improvement of regioregularity and energy band gap. *RSC Adv.* **8**, 8319-8328 (2018).

22 Herod, T. E. & Schlenoff, J. B. Doping-induced strain in polyaniline: stretchoelectrochemistry. *Chem. Mater.* **5**, 951-955 (1993).

23 Yakuphanoglu, F., Şenkal, B. F. & Saraç, A. Electrical Conductivity, Thermoelectric Power, and Optical Properties of Organo-Soluble Polyaniline Organic Semiconductor. *J. Electron. Mater.* **37**, 930-934 (2008).